

# SF-Loc: A Visual Mapping and Geo-Localization System based on Sparse Visual Structure Frames

Yuxuan Zhou, Xingxing Li\*, Shengyu Li, Chunxi Xia, Xuanbin Wang, Shaoquan Feng

**Abstract**—For high-level geo-spatial applications and intelligent robotics, accurate global pose information is of crucial importance. Map-aided localization is a generally applicable approach to overcome the limitations of global navigation satellite system (GNSS) in challenging environments. However, current solutions face challenges in terms of mapping efficiency, storage burden and re-localization performance. In this work, we present SF-Loc, a lightweight visual mapping and map-aided localization system, which is built upon the image-based map representation with dense but compact depth, termed as visual structure frames. In the mapping phase, multi-sensor dense bundle adjustment (MS-DBA) with global optimization is applied to construct geo-referenced visual structure frames. Besides, a co-visibility-based mechanism is developed to achieve incremental mapping and keep the map sparsity. In the localization phase, coarse-to-fine vision-based localization is performed, in which multi-frame information and the map distribution are fully leveraged. To be specific, spatiotemporally associated similarity (SAS) is proposed to overcome the place ambiguity, and pairwise frame matching is applied for robust pose estimation. Experimental results on the real-world cross-temporal dataset verify the effectiveness of the system. In complex urban road scenarios, the map size is down to 3 MB per kilometer and stable decimeter-level re-localization can be achieved.

**Index Terms**—Dense bundle adjustment, multi-sensor fusion, visual localization and mapping, place recognition

## I. INTRODUCTION

Global localization is a critical problem in robotics and autonomous driving applications [1], [2]. For outdoor scenarios, global navigation satellite system (GNSS) is a commonly used technology for achieving global drift-free localization [3]. However, precise GNSS generally relies on high-precision services and products, while low-cost GNSS can hardly provide stable and accurate localization solutions in complex environments [4]. Map matching is another method for global localization. By associating observations from exteroceptive sensors (such as cameras) mounted on intelligent devices with the prior maps, different levels of global localization can be achieved, depending on the map representation [5], [6].

To achieve the practicality of map-aided localization, both mapping and re-localization need to be handled. As to the

This work was supported by the National Science Fund for Distinguished Young Scholars of China (42425401), the National Natural Science Foundation of China (423B2401), the National Key Research and Development Program of China (2023YFB3907100), and the China Postdoctoral Science Foundation-Hubei Joint Support Program (2025T041HB). The numerical calculations in this paper have been done on the supercomputing system at the Supercomputing Center of Wuhan University. (Corresponding author: Xingxing Li.)

The authors are with School of Geodesy and Geomatics, Wuhan University, China (e-mail: xingxingli@whu.edu.cn).

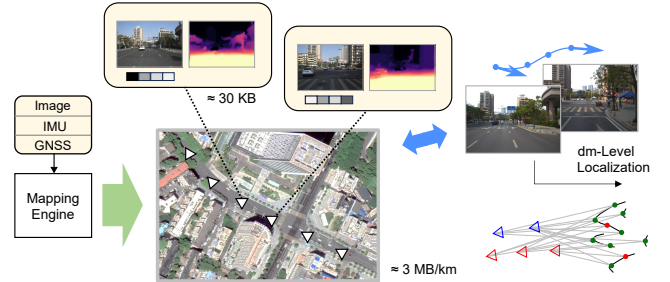


Fig. 1. Illustration of the SF-Loc system. The system is built upon the map representation of visual structure frames, which contain compressed image, compact depth information and global descriptor. The map sparsity is intentionally maintained, which ensures lightweight storage ( $\approx 3$  MB/km) while keeps the ability of high-recall, decimeter level re-localization.

mapping phase, the efficiency of map construction, the map accuracy, the storage burden and the information sufficiency for localization are some of the key factors. Current map forms, like vector map [7], 3D point cloud [8], [9], occupancy grid [10] and neural representations [11], [12], still cannot fully satisfy all these requirements simultaneously, especially when considering vision-based low-cost schemes.

As to re-localization, the system functionality is highly coupled with the map data. High recall and high localization accuracy generally need more detailed and distinguishable information of the environment, which seems contradictory with the expectation of a lightweight map.

It is noted that, the image itself can serve as an advantageous landmark for localization-oriented maps, which is rich in cues for fine-grained association, widely accessible on ubiquitous devices, and free from cross-modality information loss. However, the following issues should be considered:

- 1) How to efficiently and accurately recover the absolute poses of images at a large scale?
- 2) Since images are storage-intensive, to what extent can such image maps be compressed (or sparsified) while still meeting user localization requirements?
- 3) What auxiliary information is needed for accurate localization? And how to achieve high-recall localization in cross-temporal or weak-recognizability scenarios?

In this work, we propose SF-Loc (as shown in Fig. 1), a lightweight visual mapping and map-aided localization system based on sparse visual structure frames, aiming to comprehensively address the above issues. The visual structure frame is defined as a geo-tagged image frame with full-view depth, which itself supports standalone and flexible re-localization. Based on the concept, SF-Loc provides a holistically designed framework for efficient, accurate mapping and high-

availability re-localization. The contributions of the paper are as follows:

1) We provide a pipeline for large-scale mapping based on the visual-structure-frame map representation, which extracts accurate geometric information from global optimized multi-sensor dense bundle adjustment (MS-DBA) and supports the generation (incremental, multi-session, etc.) of practical localization-oriented maps.

2) We provide a coarse-to-fine map-aided localization pipeline based on the structure frame map, which leverages the spatiotemporally associated similarity (SAS) and pairwise frame matching for high-recall localization.

3) Real-world, cross-temporal experiments are conducted to validate different phases of the system.

4) The code is made open-source<sup>1</sup> to benefit the community.

## II. RELATED WORK

### A. VSLAM with multi-sensor fusion

Visual simultaneous localization and mapping (SLAM), which has been extensively studied in the past decade, is considered an effective and low-cost solution for relative pose estimation and mapping. By integrating IMU [13], [14], GNSS [3], and other sensors [15], the practicality of VSLAM can be improved in terms of robustness, continuity, accuracy and geo-referencing functionality. On this basis, multi-session and multi-agent SLAM systems are developed [16], [17]. Learning-based VSLAM frameworks are also investigated in recent implementations, covering neural/learnable representations including neural radiance fields (NeRF) [18] and 3D Gaussian splatting (3DGS) [19], data-driven association [20]–[22] and end-to-end pipelines [23]. However, to extract a practical reusable map from multi-sensor integrated VSLAM is still an open problem, especially when considering absolute accuracy and cross-temporal functionality.

### B. Visual place recognition

Visual place recognition (VPR) is a long-existing problem, which plays a crucial role in loop closure, multi-session mapping, re-localization and so on. Early approaches use handcrafted models (like bag-of-words [24] and VLAD [25]) to aggregate local feature descriptors, thus to evaluate the place similarity. To overcome the long-term change challenge, sequential information is utilized [26].

In the last decade, deep neural network (DNN)-based methods, like NetVLAD [27] and its successors with stronger backbones [28], [45], have greatly improved the practicality and accuracy of VPR. CosPlaces [29] models place recognition as classification, which enables large-scale training and is further enhanced with better viewpoint robustness [30]. AnyLoc [31] utilizes the visual foundation model to achieve ubiquitous VPR for different scenarios. It is noted that, most existing methods rarely exploit user-side temporal cues and database spatial structure, which could serve as powerful information to improve the stability of VPR.

<sup>1</sup><https://github.com/GREAT-WHU/SF-Loc>

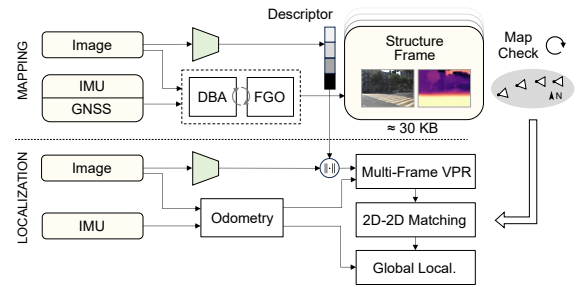


Fig. 2. The overall pipeline of the system, which is divided into the mapping phase and the localization phase.

### C. Fine-grained visual re-localization

For high-accuracy visual re-localization (e.g. decimeter- or centimeter-level), it is generally needed to perform fine-grained association between user perception and the map elements. Many of these methods follow a coarse-to-fine pipeline. In ORB-SLAM3 [8] and VINS-Mono [13], re-localization is performed through bag-of-words-based place recognition and point-level matching between feature observations and the point cloud map. Such pipeline is further improved in HLoc [9], where DNN-based models are fully utilized. Besides, monocular depth prediction is exploited in [33] to achieve map-free visual re-localization.

Other approaches try to exploit higher-level information for map matching, including instance-level object modeling [34], [35], bird's-eye view (BEV) features [36] and so on. The tradeoff of such semantic-based re-localization is the loss of detailed, sometimes subtle but distinguishable, visual cues, which might lead to higher ambiguity.

Moreover, relocalization based on neural/learnable representations (e.g., NeRF, 3DGS) has recently attracted attention. However, existing work usually focuses on small scenes [11], [12] or image pose regression within the same sequence used for model construction [37], lacking practical studies on large-scale map-based geo-localization.

## III. SYSTEM OVERVIEW

The proposed system is mainly divided into the mapping phase and the localization phase, as shown in Fig. 2.

In the mapping phase, multi-sensor information is used to generate the feature-free map frames with recovered dense depth. Global optimization which incorporates local visual constraints is performed periodically at low frequency to achieve optimal pose estimation. On this basis, the local co-visibility is checked to keep the map sparsity and to achieve incremental mapping. Besides, a DNN-based VPR model is employed to compute the global descriptors of map frames.

In the localization phase, deep VPR and feature matching models are exploited to achieve coarse-to-fine localization. During this process, user-side multi-frame information and the map frame distribution are fully leveraged to improve the recall rate and the accuracy.

## IV. MAPPING PHASE

In this section, the implementation details of the mapping phase are presented.

### A. Multi-Sensor Dense Bundle Adjustment

The foundation of the mapping process is to obtain accurate geometric information, i.e. the absolute poses and dense depths of the images. To achieve this, multi-sensor dense bundle adjustment (MS-DBA) with global optimization is employed.

The concept of dense bundle adjustment (DBA) is proposed in [21]. Specifically, sequential images are fed into a convolutional neural network (CNN) with gated recurrent units (GRUs) to compute dense optical flows among co-visible image pairs. To explain this, consider the rigid flow produced by dense projection of one image pair (source frame  $i$  projected to target frame  $j$ )

$$\mathbf{u}_{ij} = \Pi_c(\mathbf{T}_{ij} \circ \Pi_c^{-1}(\mathbf{u}_i, \lambda_i)), \quad \mathbf{T}_{ij} = \mathbf{T}_j \circ \mathbf{T}_i^{-1} \quad (1)$$

where  $\Pi_c$  is the camera projection model,  $\mathbf{T}_{ij}$  is the relative camera pose which lies in the 3D special Euclidean group SE(3), “ $\circ$ ” is the transformation operation of SE(3),  $\mathbf{u}_i$  denotes the  $n = (H/8) \times (W/8)$  grid-like 2D points in the image frame which balance scene structure completeness and computational cost,  $\lambda_i$  is the inverse depth map.

The optical flow module takes the rigid flow and the CNN-encoded image feature map as input and outputs the corrected optical flow (in the residual form) together with the weight  $w_{ij}$ , leading to the following linearized error equation

$$(\delta \mathbf{u}_{ij})_{2n \times 1} = [\mathbf{J}_i \quad \mathbf{J}_j \quad \mathbf{J}_{\lambda_i}] \begin{bmatrix} \xi_i^\top & \xi_j^\top & (\delta \lambda_i)_{n \times 1}^\top \end{bmatrix}^\top \quad (2)$$

where  $\xi_i, \xi_j$  are Lie algebras of the camera poses (corresponding to  $\mathbf{T}_i$  and  $\mathbf{T}_j$ ),  $\mathbf{J}_i, \mathbf{J}_j, \mathbf{J}_{\lambda_i}$  are Jacobians derived from (1).

The residual-form dense optical flows are treated as re-projection errors, which are used for bundle adjustment to simultaneously estimate the poses and dense depths of the images. This process is recurrently performed and is end-to-end trainable, which shows good generalization in real-world scenes with synthetic training [21].

In our early work [40], we demonstrate the possibility of tightly integrating DBA with multi-sensor information. To be specific, the Hessian form of Eq. (2) is derived and stacked for all projections from frame  $i$ , leading to

$$\begin{bmatrix} \mathbf{v}_i \\ \mathbf{z}_i \end{bmatrix} = \begin{bmatrix} \mathbf{B}_i & \mathbf{D}_i \\ \mathbf{D}_i^\top & \mathbf{C}_i \end{bmatrix} \begin{bmatrix} \xi_{i,1,2,\dots,N} \\ \delta \lambda_i \end{bmatrix} \quad (3)$$

where  $\mathbf{B}_i, \mathbf{C}_i, \mathbf{D}_i$  are block matrices of the Hessian matrix,  $\xi_{i,1,2,\dots,N}$  is the stacked Lie algebras of camera poses.

The dense depth states are further eliminated through Schur complement to construct a compact constraint among the poses, following

$$\underbrace{(\mathbf{B}_i - \mathbf{D}_i \mathbf{C}_i^{-1} \mathbf{D}_i^\top)}_{\mathbf{H}_{c,i}} \xi_{i,1,2,\dots,N} = \underbrace{\mathbf{v}_i - \mathbf{D}_i \mathbf{C}_i^{-1} \mathbf{z}_i}_{\mathbf{v}_{c,i}} \quad (4)$$

in which  $\mathbf{C}_i$  is a diagonal matrix.

The Hessian-form pose constraint Eq. (4), which embeds the DBA information of co-visible images, is fed to a factor graph based on GTSAM [39] for multi-sensor fusion, as shown in Fig. 3. A generic sliding-window graph design is employed, which allows for flexible integration of different sensor information. The states  $\mathbf{x}$  in the graph are as follows

$$\mathbf{x} = \{\mathbf{x}_k \mid k \in \mathcal{K}\}, \quad \mathbf{x}_k = (\mathbf{T}_{b_k}^w \quad \mathbf{v}_{b_k}^w \quad \mathbf{b}_k) \quad (5)$$

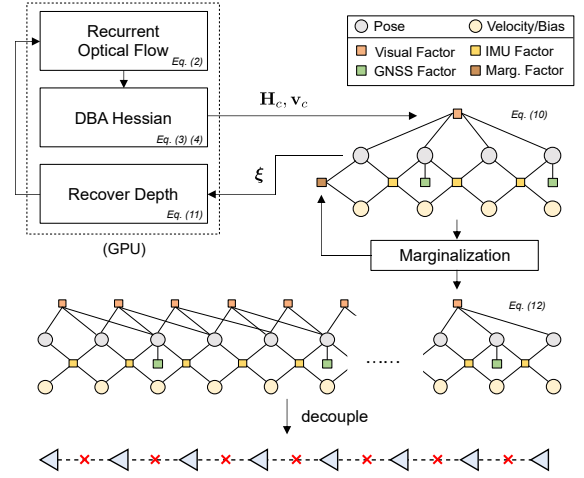


Fig. 3. Illustration of the proposed multi-sensor DBA. 1) A sliding window factor graph is used for real-time state estimation and depth estimation, which is tightly integrated with the recurrent optical flow module. 2) The global factor graph collects the marginalized factors and provides low-frequency, long-time smoothed optimization results. 3) After mature, the frames in the global factor graph are decoupled to serve as standalone visual structure frames and inserted into the map.

$$\mathbf{T}_{b_k}^w = \begin{bmatrix} \mathbf{R}_{b_k}^w & \mathbf{t}_{b_k}^w \\ 0 & 1 \end{bmatrix}, \quad \mathbf{b}_k = (\mathbf{b}_{a,k} \quad \mathbf{b}_{g,k}) \quad (6)$$

where  $\mathbf{x}_k$  is the state at time  $k$ ,  $\mathcal{K}$  represents the set of timestamps within the sliding window,  $\mathbf{T}_{b_k}^w$  is the body (IMU) poses in the world frame,  $\mathbf{v}_{b_k}^w$  is the velocity,  $\mathbf{b}_{a,k}$  and  $\mathbf{b}_{g,k}$  are accelerometer/gyroscope biases.

The following factors are considered in this work:

1) Visual factor:

$$\mathbf{E}_c(\mathbf{x}) = \frac{1}{2} l_c(\mathbf{x})^\top \mathbf{H}_c l_c(\mathbf{x}) - l_c(\mathbf{x})^\top \mathbf{v}_c \quad (7)$$

where  $\mathbf{H}_c, \mathbf{v}_c$  are the Hessian matrix and vector of DBA (stacked from  $\mathbf{H}_{c,i}, \mathbf{v}_{c,i}$  in Eq. (4)) with all the depth states eliminated,  $l_c(\cdot)$  is the linear container that transform the current states  $\mathbf{x}$  to the Lie algebras of camera poses in Eq. (4) at specific linearization point.

2) IMU factor:

$$\mathbf{r}_b(\mathbf{x}_k, \mathbf{x}_{k+1}) = \begin{bmatrix} \mathbf{R}_{b_k}^w{}^\top \left( \mathbf{p}_{b_{k+1}}^w - \mathbf{p}_{b_k}^w + \frac{1}{2} \mathbf{g}^w \Delta t_k^2 - \mathbf{v}_{b_k}^w \Delta t_k \right) - \Delta \tilde{\mathbf{p}}_{b_{k+1}}^{b_k} \\ \mathbf{R}_{b_k}^w{}^\top \left( \mathbf{v}_{b_{k+1}}^w + \mathbf{g}^w \Delta t_k - \mathbf{v}_{b_k}^w \right) - \Delta \tilde{\mathbf{v}}_{b_{k+1}}^{b_k} \\ \text{Log} \left( (\mathbf{R}_{b_k}^w)^{-1} \mathbf{R}_{b_{k+1}}^w \left( \Delta \tilde{\mathbf{R}}_{b_{k+1}}^{b_k} \right)^{-1} \right) \\ \mathbf{b}_{a,k+1} - \mathbf{b}_{a,k} \\ \mathbf{b}_{g,k+1} - \mathbf{b}_{g,k} \end{bmatrix} \quad (8)$$

where  $\Delta \tilde{\mathbf{p}}_{b_{k+1}}^{b_k}, \Delta \tilde{\mathbf{v}}_{b_{k+1}}^{b_k}, \Delta \tilde{\mathbf{R}}_{b_{k+1}}^{b_k}$  are the IMU preintegration terms [41],  $\mathbf{g}^w$  is the gravity vector,  $\Delta t_k$  is the time interval.

3) GNSS factor:

$$\mathbf{r}_g(\mathbf{x}_k) = \mathbf{T}_w^n \circ \mathbf{T}_{b_k}^w \circ \mathbf{t}_g^b - \tilde{\mathbf{p}}_g^n \quad (9)$$

where  $\tilde{\mathbf{p}}_g^n$  is the measured position of GNSS antenna in the navigation frame,  $\mathbf{t}_g^b$  is the lever-arm,  $\mathbf{T}_w^n$  is a fixed world-to-navigation transformation obtained from initial alignment.

Probabilistic marginalization [14] is applicable to the above factor graph based on Schur complement to ensure real-time

performance. Thus, the overall cost function of the sliding-window factor graph is defined as follows

$$\min \mathbf{E}_m(\mathbf{x}) + \mathbf{E}_c(\mathbf{x}) + \sum_{k \in \mathcal{K}} \|\mathbf{r}_b(\mathbf{x}_k, \mathbf{x}_{k+1})\|_{\Omega_b}^2 + \sum_{k \in \mathcal{G}} \rho_C \left( \|\mathbf{r}_g(\mathbf{x}_k)\|_{\Omega_g}^2 \right) \quad (10)$$

where  $\mathbf{E}_m(\mathbf{x})$  is the marginalization term in the quadric cost function form,  $\mathcal{G}$  is the set of GNSS measurement epochs in the sliding window,  $\Omega_b$  and  $\Omega_g$  are uncertainties of the factors,  $\rho_C(\cdot)$  is the Cauchy loss function.

After the factor graph optimization, the corrected poses are substituted back to Eq. (3) to recover the dense depths

$$\delta \lambda_i = \mathbf{C}_i^{-1}(\mathbf{z}_i - \mathbf{D}_i^\top \xi_{i,1,2,\dots,N}) \quad (11)$$

then the estimated poses and depths are fed back into the optical flow module to refine the optical flows  $\delta \mathbf{u}_{ij}$  and adjust the weights  $\mathbf{w}_{ij}$ . The overall process simultaneously adjust the pose estimation, the dense data association and the depths, trying to achieve consistency of the above information.

For mapping tasks, an issue that should be considered is the obtainment of global optimal pose estimation. In realistic scenarios, both the observability degradation of monocular visual-inertial odometry (VIO) and intermittent GNSS outages would lead to the decline of pose accuracy, which can hardly be overcome by a sliding-window estimator. To handle this, a global factor graph is maintained in our system, which collects the marginalized factors from the sliding-window factor graph for further global optimization. The objective function of the global factor graph is written as follows

$$\min \sum_{k \in \mathcal{K}_{\text{all}}} \mathbf{E}_{c,k}(\mathbf{x}_{c,k}) + \sum_{k \in \mathcal{K}_{\text{all}}} \|\mathbf{r}_b(\mathbf{x}_k, \mathbf{x}_{k+1})\|_{\Omega_b}^2 + \sum_{k \in \mathcal{G}_{\text{all}}} \rho_C \left( \|\mathbf{r}_g(\mathbf{x}_k)\|_{\Omega_g}^2 \right) \quad (12)$$

where  $\mathcal{K}_{\text{all}}$  is the set of timestamps in the global graph,  $\mathcal{G}_{\text{all}}$  is the set of all GNSS measurement epochs,  $\mathbf{E}_{c,k}(\mathbf{x}_{c,k})$  is the marginalized DBA information taking frame  $k$  as the source frame (corresponding to Eq. (4)),  $\mathbf{x}_{c,k}$  is the related poses. Each  $\mathbf{E}_{c,k}$  reflects the local visual constraint around frame  $k$ .

This global factor graph includes all the information related to the poses, velocities and IMU biases, while it can still be solved efficiently thanks to the locality of the problem. Compared to pose-only pose graph estimation (PGO) [32], this graph contains complete IMU information and Hessian-form visual information, which can better smooth low-observability periods with future information.

### B. Map Construction and Maintenance

After global pose optimization, we extract the frame pose from the global graph and form a visual structure frame by combining the JPEG-compressed RGB image, low-resolution depth map, and global descriptor from the VPR model, which is subsequently inserted into the map. To make the map lightweight, it is important to keep the sparsity of the visual structure frames without significantly compromising re-localization performance. Besides, considering the application

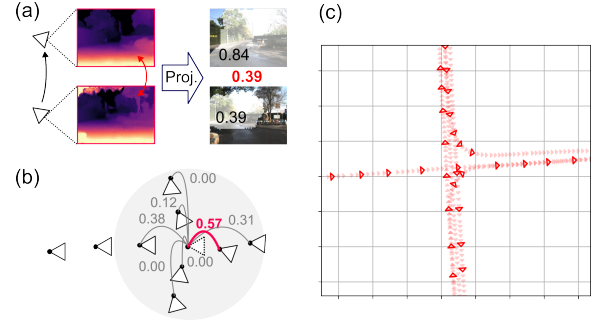


Fig. 4. Illustration of the co-visibility checking. (a) Co-visibility for one image pair; (b) Local co-visibility checking, the dashed-line frame would be added/discarded based on its score comparison with the high-covisibility map frame; (c) An example of the sparsified structure frame map.

scenario of multi-session mapping, the map should support flexible extension and update.

Fortunately, this can be simply achieved based on the model-free, frame-based map representation of SF-Loc. To be specific, the local co-visibility is checked to preserve essential frames in the map. With the global poses and dense depths, the co-visibility is efficiently computed based on the bi-directional dense rigid flow that falls within the field of view, following

$$\tau(\mathbf{T}_i, \mathbf{T}_j, \lambda_i) = \frac{\text{count}(\mathbf{u}_{ij}.\text{inside}(0, 0, H, W))}{H \cdot W} \quad (13)$$

$$\text{covis}(\mathbf{T}_i, \mathbf{T}_j, \lambda_i, \lambda_j) = \min(\tau(\mathbf{T}_i, \mathbf{T}_j, \lambda_i), \tau(\mathbf{T}_j, \mathbf{T}_i, \lambda_j)) \quad (14)$$

where  $\mathbf{u}_{ij}$  is the computed rigid flow in Eq. (1),  $H$ ,  $W$  are the height and width of the image. The illustration of the co-visibility is presented in Fig. 4.

The co-visibility directly reflects the overlapping of different frames. With the intention of avoiding redundant map frames, the inter-frame co-visibility is controlled under a threshold  $\Xi$ . Considering adding/removing/updating frames, the following mechanism is employed:

- 1) When the mapping vehicle passes through a place and generates a new map frame, existing map frames within a certain range nearby are retrieved.
- 2) The bidirectional co-visibility is checked between the new map frame and other frames.
- 3) If the bidirectional co-visibility between the new map frame and all other frames is below  $\Xi$ , add the new map frame to the map.
- 4) If there exist map frames with bidirectional co-visibility above  $\Xi$  with the new map frame, and the **score** of the new map frame is higher than that of the existing frames, delete the existing frames and add the new map frame to the map, which actually update the map locally; otherwise, discard the new map frame.

Here, the **score** can refer to metrics such as freshness, uncertainty or the proportion of dynamic objects.

It is noted that the map update mechanism is not designed to achieve the most complete scene coverage but to provide relatively large coverage with low redundancy. Under different considerations, different score metrics and update policies can be employed. The co-visibility threshold  $\Xi$  directly controls the map sparsity, which reflects the trade-off between data size and re-localization performance. We select  $\Xi = 0.4$  as

the typical value, which indicates that for one query along the smooth trajectory between two nearby map frames, an optimistic  $(1.0 + 0.4)/2 = 0.7$  overlapping can be expected.

When adding/removing/updating frames in the map, it is not necessary to perform data association across nearby frames or reconstruct the 3D model, as every visual structure frame works fully independently. This makes the mapping phase highly flexible, and can be easily applied to multi-session mapping or incremental map updating.

## V. MAP-AIDED LOCALIZATION PHASE

In this section, the implementation details of the map-aided localization are presented, which follows the coarse-to-fine process like [9]. Based on state-of-the-art place recognition and feature matching models, specially designed methods which consider spatiotemporal association are proposed to align with the map representation and to maximize the performance in realistic scenarios.

### A. Multi-Frame Place Recognition

We use lightweight CNN-based methods (e.g., [27], [29], [30], [45]) to compute global descriptors and to evaluate the similarity between the query image and map frames. On this basis, we develop a model-driven technique to integrate sequential queries and map frame distribution to improve the robustness and stability of the coarse localization.

The necessity of multi-frame place recognition lies in the existence of repetitive and featureless scenes in the real world, which leads to inevitable spatial ambiguity. To handle this, it is natural to take into account the environmental cues within a larger range to resolve the ambiguity. Notice that we call this process “multi-frame place recognition” rather than “sequential place recognition”, as the map frames are generally not “sequential” but are “randomly” distributed in the geographic space. Especially for multi-session mapping or at intersections, the spatially nearby map frames may come from multiple non-consecutive sequences.

To avoid the ambiguity of single-shot VPR, we propose a metric called spatiotemporally associated similarity (SAS) that combines the information of appearance similarity, map distribution and user-side relative poses. To be specific, we set particles around every landmark frames in the map, with every particle to be a 2D pose  $(x, y, \theta)$  that represents a candidate of the query pose. With the help of the user-side odometry, we compute the virtual trajectory of every particle, following

$$(\mathbf{T}^i)_{4 \times 4 \times L} = \mathbf{T}_{p_i}^w \left\{ \mathbf{T}_{c_{k+1-j}}^{c_k} \right\}_{j=1,2,\dots,L}, i \in \mathcal{P} \quad (15)$$

where  $\mathbf{T}_{p_i}^w$  is the particle pose,  $(\mathbf{T}^i)_{4 \times 4 \times L}$  is the virtual trajectory,  $\mathcal{P}$  is the set of particle candidates,  $L$  is the window size used for multi-frame VPR.

For every virtual trajectory, we efficiently search for the spatially nearest map frame corresponding to every history pose through KD-Tree, as shown in Fig. 5. This leads to a sequence of L2 distances for every particle

$$(\text{idx}^i)_{L \times 1} = \text{db.nearest}(\mathbf{T}^i), i \in \mathcal{P} \quad (16)$$

$$(\boldsymbol{\sigma}^i)_{L \times 1} = \boldsymbol{\sigma} [\text{idx}^i], i \in \mathcal{P} \quad (17)$$

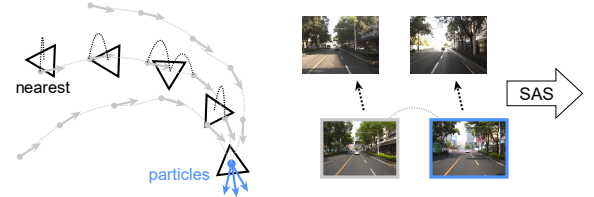


Fig. 5. Illustration of the multi-frame place recognition. Particles that indicate the query pose are set around map frames. The user-side trajectory is used for nearest searching to associate with the map frames, then the SAS distance is evaluated, which combines the information of multiple image pairs.

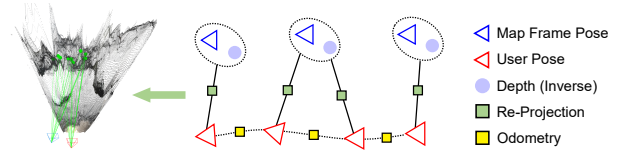


Fig. 6. Illustration of the multi-frame fine localization. Pairwise query-to-map correspondences are computed and stored to construct a factor graph, in which the depth uncertainty and matching errors can be carefully handled.

where  $\text{db}$  is the map database organized by a spatial KD-Tree for fast searching,  $\boldsymbol{\sigma}$  is the  $L \times M$  similarity matrix which stores the L2 similarities between the  $L$  query frames and all  $M$  frames in the map, “[ $\cdot$ ]” is the indexing operator. The similarity computation is performed every time a new query frame comes and stored in the memory,

Then, we compute the SAS distance by averaging the L2 distances

$$\sigma_{\text{SAS}}^i = \|\boldsymbol{\sigma}^i\|/\sqrt{L}, i \in \mathcal{P} \quad (18)$$

and the particle with minimum  $\sigma_{\text{SAS}}^i$  is taken as the retrieved map frame.

The rationale of SAS is based on the assumption that the historical images of a correctly relocalized query should also exhibit high similarity to their spatially adjacent map frames, which helps overcome the multi-peaked characteristic of descriptor-based place similarity evaluation function. The geographical distribution of map frames, along with user-side pose information, is implicitly incorporated into the metric in nearest neighbor search. In this way, the spatiotemporal association is naturally achieved, without the need of an exact sequence-to-sequence matching. This technique can be easily adopted to common VPR models without extra layers or finetuning, transforming single-frame VPR similarities to multi-frame ones, which effectively broaden the perceived context for more discriminative recognition.

In our implementation for outdoor environments, we simply set 3 particles around every map frame, corresponding to the 2D poses  $(0, 0, 0^\circ)$ ,  $(0, 0, -30^\circ)$ ,  $(0, 0, 30^\circ)$  relative to the map frame pose, which aligns with the  $60^\circ$  camera FOV and helps overcome the possible heading inconsistency of user/map frame poses.

### B. Fine Pose Estimation

After successful retrieval of the map frame corresponding to the query image, fine-grained re-localization can be performed.

Specifically, 2D-2D matching between the query and map frames is performed based on either feature-based methods

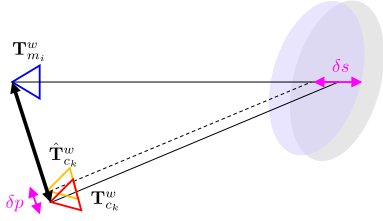


Fig. 7. Illustration of how depth uncertainty of the map frame affects the user pose estimation accuracy. In the figure,  $\delta s$  denotes the scale uncertainty of the depth map,  $\delta p$  denotes the position error of user-side localization. An approximate  $\delta p \propto \delta s \cdot |t_{c_k}^{m_i}|$  relationship can be found.

[43] or detector-free methods [48]. With these correspondences and the full-view depth contained in the map frame, several techniques can be applied to estimate the pose of the query image, like perspective-n-point (PnP) or just aligning the two-view reconstruction result with the metric-scale depth.

Despite the simplicity, the above methods couldn't be directly used for multi-frame matching. In the application scenarios that our system concerns (cross-temporal, significant appearance variation, dynamic objects, etc.), robust feature matching is hard to promise. To provide accurate pose estimation under numerous outliers, we combine multi-frame correspondences and the odometry in a factor graph, as shown in Fig. 6. For better efficiency, we don't do exhaustive matching among all the related frames. Instead, we compute the correspondences between every query-to-database image pair from VPR. Based on the re-projection errors, the cost function of the multi-frame pose estimation is written as follows

$$\begin{aligned} \min \sum_{k \in \mathcal{K}} & \left\| \mathbf{T}_{c_{k+1}}^w \circ \mathbf{T}_{c_k}^w \circ \tilde{\mathbf{T}}_{c_{k+1}}^{c_k} \right\|_{\Omega_p}^2 + \sum_{k \in \mathcal{K}} \sum_{f \in \mathcal{F}_{k,i}} \left\| \lambda_f^{m_i} - \tilde{\lambda}_f^{m_i} \right\|_{\Omega_\lambda}^2 \\ & + \sum_{k \in \mathcal{K}} \sum_{f \in \mathcal{F}_{k,i}} \rho_C \left( \left\| \Pi_c \left( \mathbf{T}_{m_i}^{c_k} \circ \Pi_m^{-1}(\mathbf{u}_f^{m_i}, \lambda_f^{m_i}) \right) - \mathbf{u}_f^{c_k} \right\|_{\Omega_c} \right) \end{aligned} \quad (19)$$

where  $\tilde{\mathbf{T}}_{c_{k+1}}^{c_k}$  is the relative pose estimation from the odometry,  $\tilde{\lambda}_f^{m_i}$  is the sampled inverse depth of point  $f$  on the fixed map frame  $m_i$ ,  $\mathcal{F}_{k,i}$  is the matched feature point set between map frame  $m_i$  and user-side frame  $c_k$ ,  $\mathbf{u}_f^{m_i}$  and  $\mathbf{u}_f^{c_k}$  are the point coordinates respectively,  $\Omega_p$ ,  $\Omega_\lambda$ ,  $\Omega_c$  are the uncertainties.

Another concern about the re-localization is whether the depth derived by monocular DBA sufficient for precise re-localization. An intuitive example is illustrated in Fig. 7. As is shown, the re-localization error is proportional to the product of the depth error (simplified as scale error) and the recall distance. In vehicle-based multi-view triangulation, it is a moderate assumption to expect  $<10\%$  depth estimation uncertainty for objects within 50 m distance in most regions of the field of view (FOV). Given 10% depth error of the map frame and  $<10$  m recall distance, we can still expect a  $<1$  m re-localization accuracy, which is adequate for our purposes. For the demand of robust re-localization, correct image retrieval and feature matching matter more than the accuracy of structure information, allowing us to store the map frame depth in a highly compact way (i.e.,  $\times 8$  downsampled, which naturally aligns with the DBA process Eq. (1)).

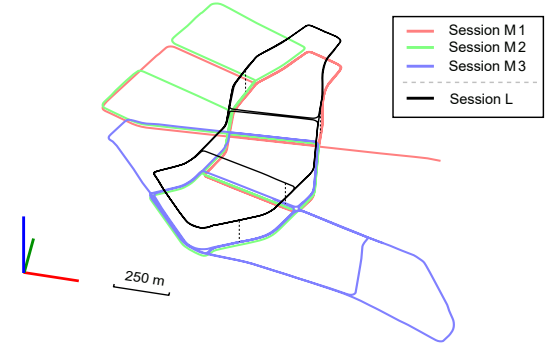


Fig. 8. Vehicle trajectories and example images of the experimental dataset. Three 1800-sec data sequences collected in 2022/10/23 (30 km mileage, 16 km one-way road coverage in total) are used for multi-session mapping, while the 1800-sec data sequence collected in 2023/04/12 (10 km mileage, 4.9 km one-way road coverage) is used for localization. Different trajectories are offset in the Z-direction to provide clearer visualization.

## VI. EXPERIMENTS

In the experimental part, different modules of the system, including multi-sensor mapping, place recognition and fine re-localization are comprehensively tested.<sup>2</sup>

To fully evaluate the mapping and localization performance of the system in complex conditions, we use the self-made dataset collected in Wuhan City on 2022/10/23 and 2023/04/12, featuring large scale, complete sensor coverage and reliable ground truth. Specifically, three data sequences on 2022/10/23 are used to evaluate the performance of incremental mapping, which provides relatively complete coverage of the region's road segments and exhibits multiple revisits. The data sequence on 2023/04/12 is used to evaluate the map-aided localization. Some challenging conditions are shown in Fig. 8, including exposure difference, occlusion, scene change and repetitive patterns.

The experimental vehicle is equipped with RGB cameras, an ADIS16470 IMU, a Septentrio AsteRx4 GNSS receiver and a tactical-grade IMU for reference use. The FOVs of the images used for mapping and localization are different ( $60^\circ$  vs.  $57^\circ$  horizontally). A nearby base station is used for differential GNSS (DGNSS) processing. The smoothed trajectory of post-processing DGNSS/INS integration based on high-end IMU is taken as the ground truth, which is featured with centimeter-to-decimeter level position accuracy.

In the mapping phase, 5 Hz images ( $512 \times 384$ ) are used. In the localization phase, 1 Hz images ( $512 \times 384$ ) are used. For multi-frame localization, except for the current frame, almost stationary frames are skipped. Considering the practical requirements of geo-localization applications, the focus is solely on horizontal positioning accuracy.

<sup>2</sup>All pretrained models and datasets are used under their respective licenses.

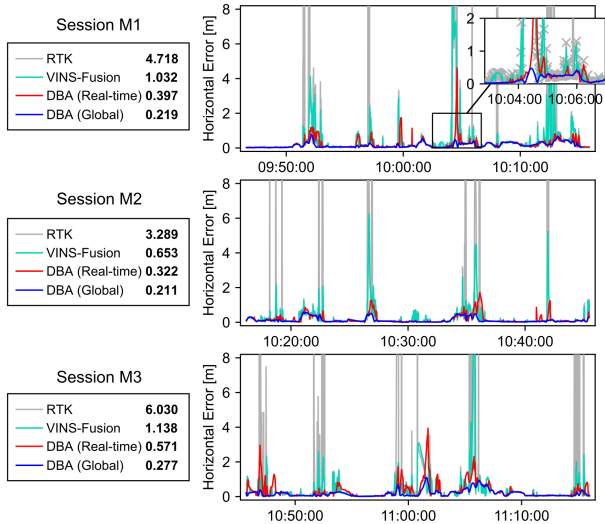


Fig. 9. Pose estimation results of the mapping phase. Monocular schemes are used for vision-based methods. The bold numbers are root mean square errors (RMSE) of the horizontal position estimation.

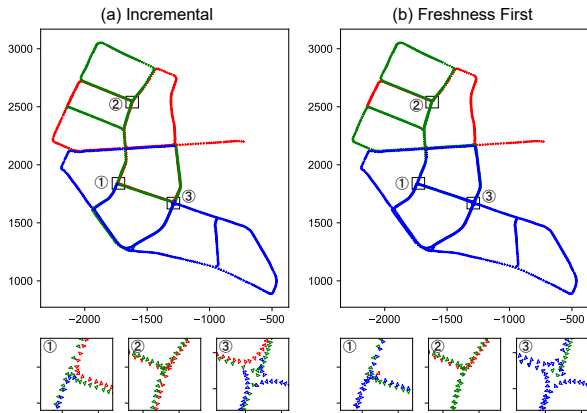


Fig. 10. Multi-session mapping results (co-visibility threshold  $\Xi = 0.4$ ) with different policies. (a) **Incremental**: In this mode, the frames of newer sessions have same scores with the old frames, thus the map would only be extended when new viewpoints are available. (b) **Freshness first**: In this mode, the frames of newer sessions have higher scores than the old frames, and the map would be updated when the vehicle passes through pre-built roads in newer sessions.

### A. Mapping Performance

We first focus on the effectiveness of the mapping phase. The data of different sessions are processed separately.

For large-scale mapping, obtaining accurate global poses is fundamental. Nevertheless, this is a challenging task considering the intermittent degradation of GNSS observations in the experimental scenario. In Fig. 9, we show the pose estimation results of different approaches, including: 1) GNSS RTK, 2) VINS-Fusion (monocular VIO + RTK, final optimized trajectory) and 3) the proposed multi-sensor DBA scheme in real-time mode and global mode respectively.

The results shown in Fig. 9 demonstrate that the DBA (global) scheme offers effective resilience to GNSS and VIO degradation, providing improved performance compared to VINS-Fusion and DBA (real-time) with RMSE reductions of 75.0% and 45.2% respectively. With the global optimization presented in Sect. IV-A, the position estimation error the DBA

TABLE I  
MAP STORAGE OF DIFFERENT MAPPING SCHEMES. FOR SF-LOC, DIFFERENT CO-VISIBILITY THRESHOLDS ( $\Xi = 0.4/0.3$ ) ARE CONSIDERED. IN CALCULATING THE DISTANCE, NON-REPEATING ONE-WAY ROADS ARE CONSIDERED.

Map Scheme	Storage (MB)	Storage per Km (MB)	Frame Number	Average Distance (m)
ORB_SLAM3	6590.51 <sup>1</sup>	403.53	18768	0.870
HLoc (SuperPoint)	32206.7 <sup>2</sup>	1971.99	27026	0.607
<b>SF-Loc</b> ( $\Xi=0.4$ )	48.473 <sup>3</sup>	2.967	1727	9.46
<b>SF-Loc</b> ( $\Xi=0.3$ )	33.007 <sup>4</sup>	2.021	1172	13.94

<sup>1</sup> 1439 MB (Local Desc.) + 719.6 MB (Global Desc.) + 4431 MB (Model)

<sup>2</sup> 27261 MB (Local Desc.) + 106.7 MB (Global Desc.) + 4839 MB (Model)

<sup>3</sup> 37.37 MB (JPEG, 60) + 3.37 MB (Global Desc.) + 7.72 MB (Depth)

<sup>4</sup> 25.47 MB (JPEG, 60) + 2.29 MB (Global Desc.) + 5.24 MB (Depth)

(global) scheme is mostly kept to decimeter-level throughout the sequence, which ensures the reference accuracy for user-side absolute localization.

Based on the global poses and dense depths, co-visibility-based multi-session mapping is performed. The distribution of generated map frames following different policies are shown in Fig.10. The results demonstrate the effectiveness and flexibility of the proposed method in performing low-redundancy mapping under different criteria. In later discussions, we simply use the map generated in “incremental” mode for evaluation.

Furthermore, the generated map data is analyzed. As baselines, we test ORB\_SLAM3 and HLoc for comparison, which are both commonly used pipelines for visual mapping and re-localization. For methods based on neural/learnable representations (e.g., NeRF [11], 3DGS [12], [37]), as existing implementations lack support for such large-scale data (30 km length) and are not directly applicable to geo-localization tasks, they are not included in the evaluation. For ORB\_SLAM3, we use the monocular visual-inertial mode to process the sequence and save the map data in the Atlas format. The map storage is over 6 GB for the whole sequence, which is relatively heavy for practical applications. As for HLoc, we found it hard to achieve such large-scale SfM through the default COLMAP [46] pipeline. Instead, we directly use the ground-truth camera poses and perform feature extraction, matching and triangulation based on Superpoint [42] and SuperGlue [44]. The map storage is over 30 GB, which is 5 times larger than the ORB\_SLAM3 map. Such heavy map makes it hard to be applied to large-scale scenarios.

As for SF-Loc, the map storage is much lighter. As mentioned in Sect. IV-B, the co-visibility threshold  $\Xi$  directly controls the map sparsity. We test different co-visibility thresholds (0.3 or 0.4) for map construction, which correspond to different sparsities with necessary consideration of scene coverage completeness. The final data size of the map is around 3 MB per kilometer for  $\Xi = 0.4$  and around 2 MB per kilometer for  $\Xi = 0.3$ , which is 1~3 orders of magnitude smaller than that of the aforementioned methods. It is noted that we use JPEG compression (quality = 60) for RGB storage and PNG compression (16 bit) for depth storage, which balances the data size and localization accuracy. Later, we will discuss how high-precision localization can be achieved under such sparsified and compressed map information.

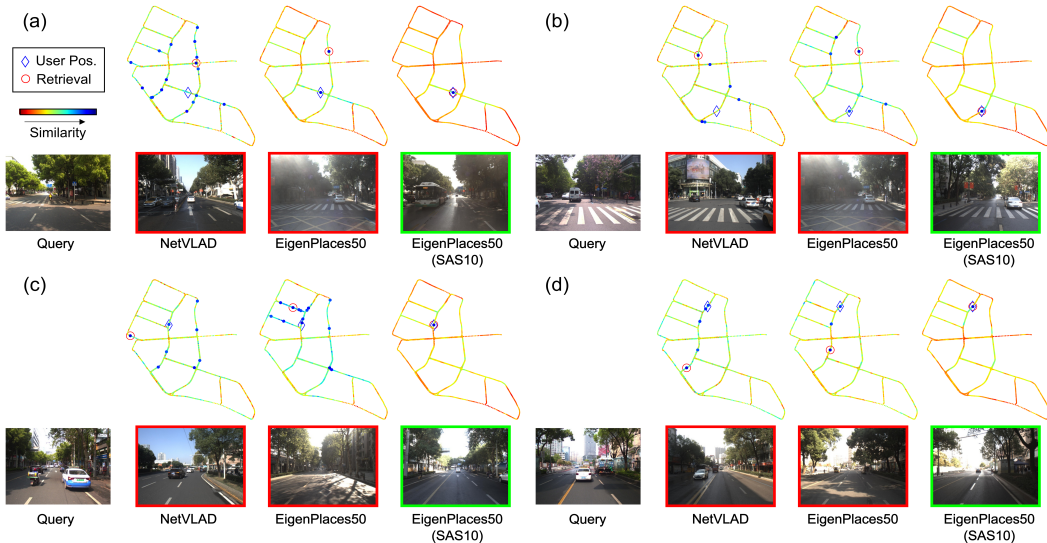


Fig. 11. Example cases of the coarse localization ( $\Xi = 0.4$ ). The green borderline indicates correct retrieval, while the red borderline indicates wrong retrieval (large position error or heading error). High-similarity candidates (local minima and  $\sigma < \sigma_{\min} + 0.15(\sigma_{\max} - \sigma_{\min})$ ) are marked using larger circles.

### B. Localization Performance

As to user-side localization, we check the coarse-to-fine localization performance of the proposed system. Considering realistic cases of localization query, we test single-frame and multi-frame (with temporal fusion) localization performance, while historical prior information (like Kalman filtering) is not considered.

1) *Coarse Localization*: The test of coarse localization is based on the map frames generated by SF-Loc. The coarse localization performance directly affects further fine-grained association, and a  $< 20$  m recall distance is generally needed for possible fine localization under the experimental scenario. We show the recall rates of different schemes in TABLE II, including the classic ORB + DBoW2 implementation [8] and DNN-based methods (NetVLAD [27], AnyLoc [31], MixVPR [45], CosPlace [29], EigenPlaces [30]). For CosPlace and EigenPlaces, different backbones (ResNet18 or ResNet50 [47]) are considered. Based on the state-of-the-art lightweight model EigenPlaces, we employ the proposed SAS technique to aggregate the information of the current and last  $K$  sequential queries, termed as “EigenPlaces (SASK)”, where different window lengths are considered. To verify the effectiveness of the proposed SAS metric, we also implement a naive multi-frame VPR model by clustering the top-10 candidates of the current and last  $K$  sequential queries and choosing the candidate belonging to the largest cluster as the result, termed as “EigenPlaces ( $K$ )”.

Taking the  $\Xi = 0.4$  map as example, several typical query cases are shown in Fig. 11, which indicate the challenge of re-localization, with (a) lighting condition variation, (b) seasonal vegetation change, (c) dynamic objects, and (d) high-ambiguity environmental patterns. In such scenarios, the traditional handcrafted place recognition method (ORB + DBoW2) becomes almost useless, as the low-level intensities of the environment changes significantly for the cross-temporal sequences. For learning-based methods, the classic NetVLAD achieves 59.53% 10 m recall, while more modern methods

(e.g., CosPlace, EigenPlaces and MixVPR) can generally achieve 85% 10 m recall. Although 85% recall seems good enough for VPR, it can’t serve as a reliable information source for the localization task, especially for unmanned systems. By naively combining the VPR results of multiple frames, the 10 m/20 m recall can increase by around 1%. In contrast, with the proposed SAS-based multi-frame VPR technique, the 10 m/20 m recall increases by approximately 10%/5%. For the SAS10 scheme, the 20 m recall achieves 100% for both ResNet50 and ResNet18 backbones. Compared to single-frame VPR methods, the introduction of SAS overcomes the challenges depicted in Fig. 11 and greatly improves the reliability of the coarse localization, which is crucial for further fine localization. Essentially, the association of spatiotemporal information serves as a cross-verification mechanism, enhancing the confidence of visual cues and leading to improved place recognition performance under significant appearance changes.

We also list the results based on a sparser map with co-visibility threshold  $\Xi = 0.3$ . The recall is noticeably lower than the  $\Xi = 0.4$  case, while the EigenPlaces50 (SAS10) scheme can still achieve 92.45%/100% 10 m/20 m recall.

As extra reference, we employ the SAS technique to VPR models other than EigenPlaces. The results listed in TABLE IV verify its broad applicability and superiority over simple clustering-based multi-frame VPR.

2) *Fine Localization*: As to the evaluation of fine localization, we test the re-localization modes of ORB-SLAM3 and HLoc as the baselines, and also test GNSS-based schemes for reference, including single point positioning (SPP) and VINS-Fusion (stereo VIO + SPP).

For ORB-SLAM3 and HLoc, the coarse-to-fine localization is performed based on their own pipeline and map data (corresponding to TABLE I). For HLoc, EigenPlaces (50) is used for coarse localization and the SuperPoint + LightGlue scheme is used for fine localization.

For the proposed SF-Loc, the map data generated with different co-visibility thresholds ( $\Xi = 0.3/0.4$ ) are considered,

TABLE II  
RECALL AND ACCURACY OF THE COARSE RE-LOCALIZATION. MAPS WITH DIFFERENT SPARSITIES (CO-VISIBILITY THRESHOLD  $\Xi = 0.4/0.3$ ) ARE CONSIDERED RESPECTIVELY.

$\Xi$	Method	Recall @5 m	Recall @10 m	Recall @20 m	RMSE <sup>1</sup> (m)
0.4	ORB + DBoW2	1.28%	2.01%	2.62%	49.17
	NetVLAD	45.19%	59.53%	67.46%	15.01
	AnyLoc	59.10%	80.39%	89.73%	12.99
	MixVPR	65.89%	86.75%	95.60%	7.58
	CosPlace18	59.86%	84.41%	95.38%	8.22
	CosPlace50	61.54%	85.71%	95.55%	8.57
	EigenPlaces18	61.43%	84.57%	94.62%	8.35
	EigenPlaces50	63.88%	87.62%	97.12%	7.77
	EigenPlaces18 (5)	61.71%	85.44%	96.31%	9.28
	EigenPlaces50 (5)	64.31%	88.32%	98.21%	7.18
	EigenPlaces18 (10)	61.76%	85.61%	96.47%	8.75
	EigenPlaces50 (10)	64.48%	88.76%	98.75%	7.00
	EigenPlaces18 (SAS5)	74.69%	95.76%	99.57%	6.07
	EigenPlaces50 (SAS5)	<b>74.74%</b>	96.36%	99.89%	4.78
EigenPlaces18 (SAS10)	74.47%	<b>97.01%</b>	<b>100.00%</b>	4.65	
EigenPlaces50 (SAS10)	74.58%	96.80%	<b>100.00%</b>	<b>4.57</b>	
0.3	ORB + DBoW2	1.16%	1.77%	2.80%	47.78
	NetVLAD	34.11%	51.44%	61.60%	17.45
	AnyLoc	47.26%	76.10%	88.21%	13.82
	MixVPR	52.69%	84.46%	95.27%	8.32
	CosPlace18	50.03%	82.24%	94.79%	8.88
	CosPlace50	50.30%	82.94%	95.17%	9.57
	EigenPlaces18	51.66%	83.76%	94.73%	8.26
	EigenPlaces50	53.50%	86.04%	96.80%	8.25
	EigenPlaces18 (5)	51.93%	84.41%	95.60%	9.49
	EigenPlaces50 (5)	53.72%	86.91%	97.94%	7.97
	EigenPlaces18 (10)	51.71%	84.36%	95.71%	8.44
	EigenPlaces50 (10)	53.56%	86.64%	97.61%	7.96
	EigenPlaces18 (SAS5)	55.78%	91.80%	99.02%	6.70
	EigenPlaces50 (SAS5)	56.60%	92.29%	99.57%	6.01
EigenPlaces18 (SAS10)	<b>56.93%</b>	<b>92.50%</b>	99.78%	5.97	
EigenPlaces50 (SAS10)	56.49%	92.45%	<b>100.00%</b>	<b>5.80</b>	

<sup>1</sup> For RMSE calculation, only < 100 m cases are taken into account.

TABLE III  
RECALL OF THE COARSE RE-LOCALIZATION WITH DIFFERENT MULTI-FRAME PROCESSING TECHNIQUES BASED ON DIFFERENT VPR MODELS. THE SF-LOC MAP WITH  $\Xi = 0.4$  IS CONSIDERED.

VPR Model	Multi-Frame	Recall @5 m (%)	Recall @10 m (%)	Recall @20 m (%)
NetVLAD	-	45.19	59.53	67.46
	10	49.05 (3.86 $\uparrow$ )	66.11 (6.58 $\uparrow$ )	76.75 (9.29 $\uparrow$ )
	SAS10	69.20 ( <b>24.0</b> $\uparrow$ )	91.31 ( <b>31.8</b> $\uparrow$ )	96.31 ( <b>28.9</b> $\uparrow$ )
AnyLoc	-	59.10	80.39	89.73
	10	60.24 (1.14 $\uparrow$ )	82.07 (1.48 $\uparrow$ )	92.02 (2.29 $\uparrow$ )
	SAS10	71.92 ( <b>12.8</b> $\uparrow$ )	95.60 ( <b>15.2</b> $\uparrow$ )	99.51 ( <b>9.78</b> $\uparrow$ )
MixVPR	-	65.89	86.75	95.60
	10	66.16 (0.27 $\uparrow$ )	87.29 (0.54 $\uparrow$ )	96.52 (0.92 $\uparrow$ )
	SAS10	72.30 ( <b>6.41</b> $\uparrow$ )	96.36 ( <b>9.61</b> $\uparrow$ )	99.95 ( <b>4.35</b> $\uparrow$ )

and the coarse localization results of EigenPlaces50 (SAS10) are used. For fine localization, we test both single-frame and multi-frame modes. For multi-frame fine localization, the matching results of  $N$  sequential queries are used, and the user-side relative poses are provided by stereo VIO (about 1% relative translation error, consistent with typical performance [14]). Basically, the feature matching is performed using SuperPoint + LightGlue, and the factor graph optimization

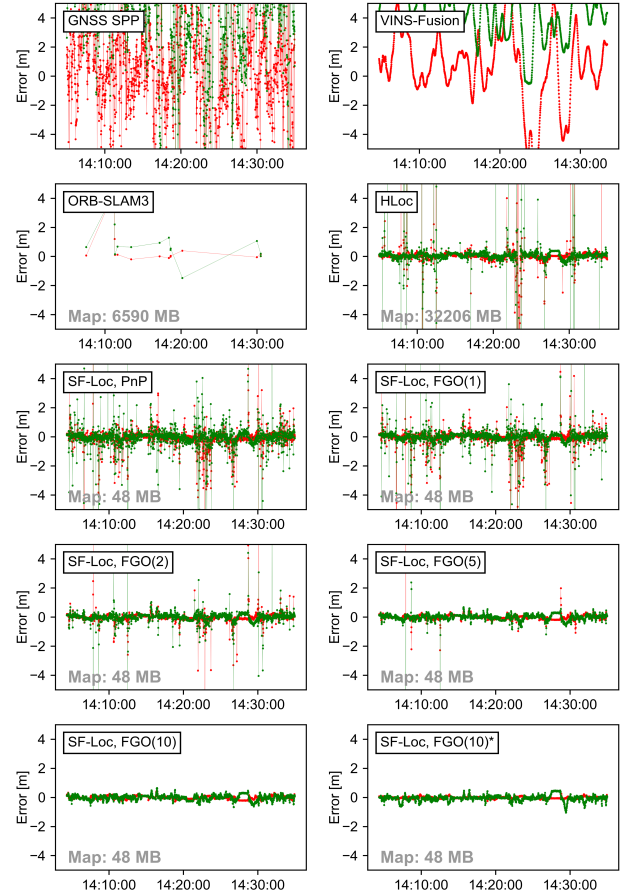


Fig. 12. Horizontal position errors of the fine localization. For SF-Loc, the  $\Xi = 0.4$  map is used and different multi-frame settings (1, 2, 5, 10) are employed. See TABLE IV for detailed description.

implementation in Sect. V-B is used. For comparison, we also test PnP with RANSAC upon the SF-Loc map.

As can be seen from Fig. 12 and TABLE IV, ORB-SLAM3 can hardly perform successful re-localization, as the feature matching based on local intensity pattern is greatly challenged by the significant appearance variation. For HLoc and SF-Loc, decimeter-level localization is achievable when the map matching is well performed, while outliers with several-meter error are also present, which indicates ambiguous data association. It is noted that HLoc performs better than single-frame SF-Loc, which is reasonable as the HLoc map contains many more frames (see TABLE I) and stores the fine descriptors extracted from lossless raw images. In contrast, SF-Loc only uses highly compressed map frame information.

It is impressive that, the localization accuracy of SF-Loc can be greatly improved by integrating multi-frame information. The examples that multi-frame observations lead to better data association and localization results are depicted in Fig. 13. As can be seen, the dynamic objects and unstable features in Fig. 13 (a), as well as the mismatches caused by repetitive textures in Fig. 13 (b), lead to significant errors in single-frame localization. The introduction of multi-frame information helps adjust the inlier set of correspondences and improve the geometric configuration, leading to more robust pose estimation. For the  $\Xi = 0.4$  map, SF-Loc with 10-frame FGO achieves

TABLE IV  
ACCURACY OF THE FINE RE-LOCALIZATION. HORIZONTAL POSITION ERRORS ARE EVALUATED.  $d_{VPR}$  DENOTES THE MEDIAN RECALL DISTANCE OF COARSE LOCALIZATION.

Map [ $d_{VPR}$ (m)]	Method <sup>1</sup>	Avail. @0.5 m	Avail. @1.0 m	Avail. @5.0 m	RMSE <sup>2</sup> (m)
-	SPP	0.11%	0.44%	19.16%	8.059
-	VINS-Fusion	0.00%	0.00%	42.92%	5.628
ORB [3.12]	ORB-SLAM3	0.44%	0.78%	1.00%	1.665
SP [2.42]	HLoc	89.56%	93.23%	96.34%	0.505
SF ( $\Xi=0.4$ ) [3.19]	PnP	72.62%	86.53%	98.15%	0.839
	FGO (1)	81.53%	90.11%	98.37%	0.722
	FGO (2)	90.98%	96.20%	99.35%	0.452
	FGO (5)	96.09%	99.40%	99.84%	0.259
	FGO (10)	<b>98.53%</b>	<b>100.00%</b>	<b>100.00%</b>	<b>0.209</b>
	FGO (10)*	96.36%	99.89%	100.00%	0.219
SF ( $\Xi=0.3$ ) [4.30]	PnP	65.73%	83.70%	97.45%	0.934
	FGO (1)	77.35%	87.29%	97.66%	0.830
	FGO (2)	86.31%	93.86%	98.91%	0.614
	FGO (5)	94.84%	98.26%	100.00%	0.306
	FGO (10)	<b>98.97%</b>	<b>100.00%</b>	<b>100.00%</b>	<b>0.198</b>
	FGO (10)*	96.54%	99.84%	100.00%	0.227

<sup>1</sup> For ORB-SLAM3, HLoc and SF-Loc without the “\*” notation, relative pose estimation between the query frame and the map frame is evaluated. The “\*” notation means that the absolute position error is evaluated, i.e., the pose error of the map frame (see Fig. 9) is taken into account.

<sup>2</sup> For RMSE calculation, only recall distance of coarse localization <20 m and final error <5 m cases are taken into account.

TABLE V  
ACCURACY OF SINGLE-FRAME FINE LOCALIZATION USING DIFFERENT MATCHING METHODS. USING “SF-LOC, FGO(1)” SCHEME ( $\Xi = 0.4$ ).

Method <sup>1</sup>	Avail. @0.5 m	Avail. @1.0 m	Avail. @5.0 m	RMSE <sup>1</sup> (m)	Time Cost (ms)
SP + LG	81.53%	90.11%	98.37%	0.722	30 + 23
AspanFormer	77.78%	87.83%	97.66%	0.882	125
RoMa	87.02%	93.59%	<b>98.90%</b>	0.719	371
LoFTR	79.58%	90.49%	97.50%	0.773	68
MASt3R	<b>89.90%</b>	<b>94.13%</b>	98.21%	<b>0.580</b>	307
MASt3R <sup>†</sup>	32.54%	52.36%	95.33%	1.601	307

<sup>1</sup> For RMSE calculation, only < 5 m cases are taken into account.

<sup>†</sup> Using predicted depth instead of the depth in the map frame.

98.53% availability@0.5 m and an RMSE of 0.209 m. As to the absolute positioning accuracy considering the error of map frames, the availability@0.5 m is 96.36% and the RMSE is 0.219 m, which mainly satisfy the demand of decimeter-level localization accuracy. When the map becomes sparser ( $\Xi = 0.3$ ), the multi-frame localization performance remains almost unchanged, which shows the possibility of harder map compression in the cost of some redundancy.

In addition, based on the feature-free map with dense depth, detector-free matching approaches can be naturally applied in SF-Loc. In TABLE V, we compare state-of-the-art detector-free matching methods [48]–[51] with the default SuperPoint + LightGlue scheme. The results demonstrate the possibility of achieving higher localization accuracy in cost of extra computational resources. We also consider a “map-free” localization strategy based on MASt3R’s metric depth prediction; However, its performance is relatively suboptimal, possibly due to domain discrepancies across datasets. This further underscores the value of incorporating metric-scale dense depth information into the visual structure frame map.

Finally, we show the time consumption statistics of user-side

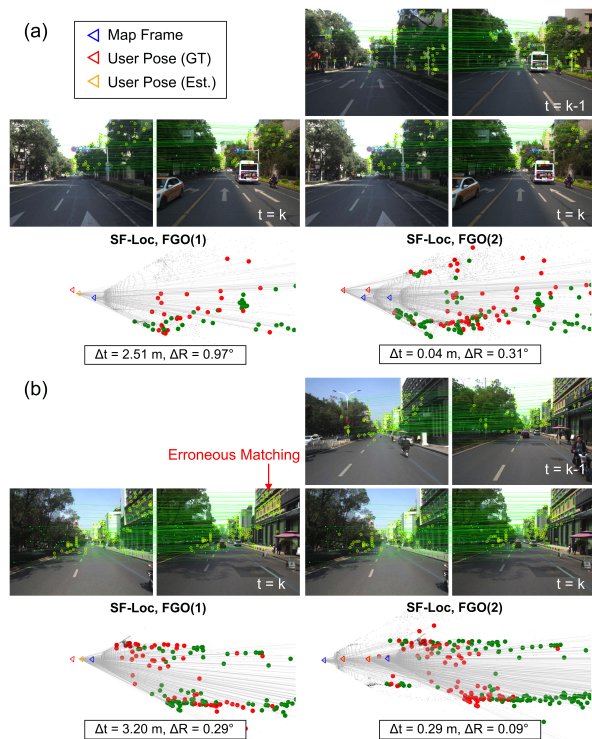


Fig. 13. Examples of fine re-localization based on single-/multi-frame observations, using “SF-Loc, FGO(1)” and “SF-Loc, FGO(2)” schemes respectively. Position and attitude errors are provided in the attached boxes.

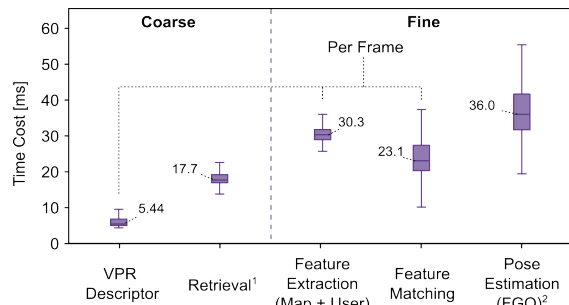


Fig. 14. Time costs of different modules in user-side localization of SF-Loc. It is noted that VPR descriptor computation, feature extraction and matching are performed every time a frame comes and stored, so it won’t lead to significant latency during multi-frame processing. <sup>1</sup> Using “EigenPlaces50 (SAS10)” scheme in TABLE II. <sup>2</sup> Using “SF-Loc, FGO(10)” scheme in TABLE IV.

localization in Fig. 14, which is tested on a laptop with Nvidia RTX 4080 Mobile GPU. With an average processing time of around 110 ms per incoming image and an input frequency of 1 Hz, the system demonstrates good real-time performance.

## VII. CONCLUSION

In this paper, we propose a vision-centered mapping and localization framework based on the map representation of visual structure frames. The highlight of the system is the lightweight map storage by making the frame data compact and keeping the sparsity, while still being able to support high-recall, high-accuracy localization through the utilization of user-side multi-frame information.

In our future work, we will extend the system to indoor scenarios, explore hybrid map representations, and further investigate the reliability issue of visual localization.

## REFERENCES

- [1] C. Cadena et al., “Past, Present, and Future of Simultaneous Localization and Mapping: Toward the Robust-Perception Age,” *IEEE Trans. Robot.*, vol. 32, no. 6, pp. 1309–1332, Dec. 2016.
  - [2] I. Ullah, D. Adhikari, H. Khan, M. S. Anwar, S. Ahmad, and X. Bai, “Mobile robot localization: Current challenges and future prospective,” *Comput. Sci. Rev.*, vol. 53, p. 100651, 2024.
  - [3] X. Li et al., “Continuous and precise positioning in urban environments by tightly coupled integration of GNSS, INS and vision,” *IEEE Robot. Autom. Lett.*, vol. 7, no. 4, pp. 11458–11465, 2022.
  - [4] W. Wen and L.-T. Hsu, “Towards robust GNSS positioning and real-time kinematic using factor graph optimization,” in *ICRA 2021*, pp. 5884–5890.
  - [5] A. Chalvatzaras, I. Pratikakis, and A. A. Amanatiadis, “A survey on map-based localization techniques for autonomous vehicles,” *IEEE Trans. Intell. Veh.*, vol. 8, no. 2, pp. 1574–1596, 2022.
  - [6] P. Yin et al., “General Place Recognition Survey: Towards Real-World Autonomy,” May 08, 2024, arXiv: arXiv:2405.04812.
  - [7] Z. Zhang et al., “BEV-Locator: An End-to-end Visual Semantic Localization Network Using Multi-View Images,” Nov. 27, 2022, arXiv: arXiv:2211.14927.
  - [8] C. Campo et al., “ORB-SLAM3: An Accurate Open-Source Library for Visual, Visual-Inertial, and Multimap SLAM,” *IEEE Trans. Robot.*, vol. 37, no. 6, pp. 1874–1890, Dec. 2021.
  - [9] P. E. Sarlin et al., “From coarse to fine: Robust hierarchical localization at large scale,” in *CVPR 2019*, pp. 12716–12725.
  - [10] L. Xu, C. Feng, V. R. Kamat, and C. C. Menassa, “An Occupancy Grid Mapping enhanced visual SLAM for real-time locating applications in indoor GPS-denied environments,” *Autom. Constr.*, vol. 104, pp. 230–245, Aug. 2019.
  - [11] D. Maggio et al., “Loc-NeRF: Monte Carlo Localization using Neural Radiance Fields,” arXiv preprint arXiv:2209.09050, 2022.
  - [12] H. Zhai et al., “SplatLoc: 3D Gaussian Splatting-based Visual Localization for Augmented Reality,” Sep. 21, 2024, arXiv: arXiv:2409.14067.
  - [13] T. Qin, P. Li, and S. Shen, “Vins-mono: A robust and versatile monocular visual-inertial state estimator,” *IEEE Trans. Robot.*, vol. 34, no. 4, pp. 1004–1020, 2018.
  - [14] S. Leutenegger et al., “Keyframe-based visual-inertial odometry using nonlinear optimization,” *IJRR*, vol. 34, no. 3, pp. 314–334, 2014.
  - [15] K. Wu, C. Guo, G. Georgiou, and S. I. Roumeliotis, “Vins on wheels,” in *ICRA 2017*, pp. 5155–5162.
  - [16] A. Cramariuc et al., “maplab 2.0—a modular and multi-modal mapping framework,” *IEEE Robot. Autom. Lett.*, vol. 8, no. 2, pp. 520–527, 2022.
  - [17] Y. Tian et al., “Kimera-multi: Robust, distributed, dense metric-semantic slam for multi-robot systems,” *IEEE Trans. Robot.*, vol. 38, no. 4, 2022.
  - [18] Z. Zhu et al., “Nicer-slam: Neural implicit scene encoding for rgb slam,” Feb. 2023, arXiv:2302.03594.
  - [19] H. Matsuki, R. Murai, P. H. Kelly, and A. J. Davison, “Gaussian splatting slam,” in *CVPR 2024*, pp. 18039–18048.
  - [20] Z. Teed, L. Lipson, and J. Deng, “Deep patch visual odometry,” in *NeurIPS 2024*.
  - [21] Z. Teed and J. Deng, “Droid-slam: Deep visual slam for monocular, stereo, and rgb-d cameras,” in *NeurIPS 2021*, pp. 16558–16569.
  - [22] S. Li et al., “Quantized Self-Supervised Local Feature for Real-Time Robot Indirect VSLAM,” in *IEEE/ASME TMEch*, vol. 27, no. 3, pp. 1414–1424, June 2022.
  - [23] S. Wang, R. Clark, H. Wen, and N. Trigoni, “Deepvo: Towards end-to-end visual odometry with deep recurrent convolutional neural networks,” in *ICRA 2017*, pp. 2043–2050.
  - [24] D. Gálvez-López, J. D. Tardos, “Bags of binary words for fast place recognition in image sequences,” *IEEE Trans. Robot.*, vol. 28, no.5, pp. 1188–1197, 2012.
  - [25] H. Jégou et al., “Aggregating local descriptors into a compact image representation,” in *CVPR 2010*, pp. 3304–3311.
  - [26] M. J. Milford and G. F. Wyeth, “SeqSLAM: Visual route-based navigation for sunny summer days and stormy winter nights,” in *ICRA 2012*, pp. 1643–1649.
  - [27] R. Arandjelović et al., “NetVLAD: CNN Architecture for Weakly Supervised Place Recognition,” *IEEE TPAMI*, vol. 40, no. 6, pp. 1437–1451, June 2018.
  - [28] R. Wang et al., “Transvpr: Transformer-based place recognition with multi-level attention aggregation,” in *CVPR 2022*, pp. 13648–13657.
  - [29] G. Berton, C. Masone, and B. Caputo, “Rethinking visual geolocalization for large-scale applications,” in *CVPR 2022*, pp. 4878–4888.
  - [30] G. Berton et al., “Eigenplaces: Training viewpoint robust models for visual place recognition,” in *ICCV 2023*, pp. 11080–11090.
  - [31] N. Keetha et al., “AnyLoc: Towards Universal Visual Place Recognition,” *IEEE Robot. Autom. Lett.*, vol. 9, no. 2, pp. 1286–1293, Feb. 2024.
  - [32] T. Qin et al., “A general optimization-based framework for global pose estimation with multiple sensors,” arXiv:1901.03642, 2019.
  - [33] E. Arnold et al., “Map-Free Visual Relocalization: Metric Pose Relative to a Single Image,” in *ECCV 2022*.
  - [34] S. Yang and S. Scherer, “Cubeslam: Monocular 3-d object slam,” *IEEE Trans. Robot.*, vol. 35, no. 4, pp. 925–938, 2019.
  - [35] Y. Yu et al., “Accurate and Robust Visual Localization System in Large-Scale Appearance-Changing Environments,” in *IEEE/ASME TMEch*, vol. 27, no. 6, pp. 5222–5232, Dec. 2022.
  - [36] P.-E. Sarlin et al., “Orienternet: Visual localization in 2d public maps with neural matching,” in *CVPR 2023*, pp. 21632–21642.
  - [37] P. Jiang, G. Pandey, and S. Saripalli, “3DGS-ReLoc: 3D Gaussian Splatting for Map Representation and Visual ReLocalization,” arXiv preprint arXiv:2403.11367, 2024.
  - [38] Wallace, Gregory K. “The JPEG still picture compression standard.” *Communications of the ACM*, vol. 34, no. 4, pp. 30–44, 1991.
  - [39] F. Dellaert and M. Kaess, *Factor Graphs for Robot Perception*. Foundations, 2017.
  - [40] Y. Zhou et al., “DBA-Fusion: Tightly Integrating Deep Dense Visual Bundle Adjustment With Multiple Sensors for Large-Scale Localization and Mapping,” *IEEE RAL*, vol. 9, no. 7, pp. 6138–6145, Jul. 2024.
  - [41] C. Forster, L. Carlone, F. Dellaert and D. Scaramuzza, “On-manifold preintegration for real-time visual-inertial odometry,” *IEEE Trans. Robot.*, vol. 33, no. 1, pp. 1–21, Feb. 2017.
  - [42] D. DeTone, T. Malisiewicz, and A. Rabinovich, “Superpoint: Self-supervised interest point detection and description,” in *CVPRW 2018*, pp. 224–236.
  - [43] P. Lindenberger, P.-E. Sarlin, and M. Pollefeys, “Lightglue: Local feature matching at light speed,” in *ICCV 2023*, pp. 17627–17638.
  - [44] P.-E. Sarlin, D. DeTone, T. Malisiewicz, and A. Rabinovich, “Superglue: Learning feature matching with graph neural networks,” in *CVPR 2020*, pp. 4938–4947.
  - [45] A. Ali-Bey, B. Chaib-Draa, and P. Giguere, “Mixvpr: Feature mixing for visual place recognition,” in *WACV 2023*, pp. 2998–3007.
  - [46] J. L. Schonberger and J.-M. Frahm, “Structure-from-motion revisited,” in *CVPR 2016*, pp. 4104–4113.
  - [47] K. He, X. Zhang, S. Ren, and J. Sun, “Deep residual learning for image recognition,” in *CVPR 2016*, pp. 770–778.
  - [48] J. Sun et al., “LoFTR: Detector-free local feature matching with transformers,” in *CVPR 2021*, pp. 8922–8931.
  - [49] H. Chen et al., “ASpanFormer: Detector-Free Image Matching with Adaptive Span Transformer,” in *ECCV 2022*, pp. 20–36.
  - [50] J. Edstedt et al., “RoMa: Robust Dense Feature Matching,” in *CVPR 2024*, pp. 19790–19800.
  - [51] V. Leroy, Y. Cabon, and J. Revaud, “Grounding Image Matching in 3D with MAST3R,” in *ECCV 2024*, pp. 71–91.
- Yuxuan Zhou** received the M.Eng. degree in navigation engineering from Wuhan University, Wuhan, China, in 2022, where he is currently pursuing the Ph.D. degree with the School of Geomatics and Geodesy. His current research interests include integrated navigation systems and multi-sensor fusion.
- Xingxing Li** received the Ph.D. degree from the Department of Geodesy and Remote Sensing, German Research Centre for Geosciences (GFZ). He is currently a Professor with Wuhan University. His current research interests include GNSS precise data processing and multi-sensor navigation.
- Shengyu Li** received the M.Eng. degree in navigation engineering from Wuhan University, Wuhan, China, in 2022, where he is currently pursuing the Ph.D. degree with the School of Geomatics and Geodesy. His current research interests include integrated navigation systems and multi-sensor fusion.
- Chunxi Xia** received the M.Eng. degree in navigation engineering from Wuhan University, Wuhan, China, in 2023, where he is currently pursuing the Ph.D. degree with the School of Geomatics and Geodesy. His current research interests include vision-based navigation and multi-sensor fusion.
- Xuanbin Wang** received the M.Eng. degree in navigation engineering from Wuhan University, Wuhan, China, in 2021. He is currently pursuing the Ph.D. degree with the School of Geomatics and Geodesy, Wuhan University. His current research focuses on integrated navigation system and multi-sensor fusion.
- Shaoquan Feng** received the M.Eng. degree in geodesy and survey engineering from Wuhan University, Wuhan, China, in 2020, where he is currently pursuing the Ph.D. degree with the School of Geomatics and Geodesy. His current research interests include multi-object tracking, integrated navigation systems, and multi sensor fusion.